Geophysical Journal International

Geophys. J. Int. (2024) **238,** 199–213
Advance Access publication 2024 April 29
GJI Rock and Mineral Physics, Rheology

https://doi.org/10.1093/gji/ggae156

Temporal evolution of shear-induced dilatancy of rock fractures: controls from surface roughness and normal stress

Supeng Zhang,[1,2,3] Yinlin Ji ,[1] Hannes Hofmann ,[1,4] Qian Yin,[5] Shouding Li[2,3] and Yuanchao Zhang[6]

[1]*Helmholtz Centre Potsdam GFZ German Research Centre for Geosciences, Section* 4.8 *Geoenergy, Telegrafenberg,* D-14473 *Potsdam, Germany. E-mail: yinlinji@gfz-potsdam.de*
[2]*Key Laboratory of Shale Gas and Geoengineering, Institute of Geology and Geophysics, Chinese Academy of Sciences, Beijing* 100029, *China*
[3]*College of Earth and Planetary Sciences, University of Chinese Academy of Sciences, Beijing* 100049, *China*
[4]*Institute of Applied Geosciences, Technische Universität Berlin, Ernst-Reuter-Platz* 1, D-10587 *Berlin, Germany*
[5]*State Key Laboratory for Geomechanics and Deep Underground Engineering, China University of Mining and Technology, Xuzhou* 221116, *China*
[6]*College of Civil Engineering, Fuzhou University, Fuzhou* 350108, *China*

Accepted 2024 April 26. Received 2024 April 22; in original form 2023 November 10

SUMMARY

Understanding the shear-induced dilatancy of rock fractures is important for assessing the permeability evolution and seismic hazard in shale and geothermal reservoirs. The displacement dependence of fracture dilation has been well studied, while the influence of slip velocity is poorly constrained. In this study, we combined displacement- and velocity-dependent aperture models to reproduce the transient shear-induced dilatancy of fractures in sandstone in 16 normal stress unloading tests. Our results show that the combined aperture model can describe the transient fracture aperture evolution during accelerating slip induced by normal stress unloading better than the model dependent only on slip displacement. Slip velocity could enhance the aperture increase on smoother fractures at lower normal stresses and higher slip velocities. Both the dilation factor and characteristic slip distance decrease with increasing normal stress and surface roughness, signifying reduced contribution of slip velocity to transient shear-induced dilatancy at higher normal stresses and surface roughness. The dilation angle increases with the increase of surface roughness, and this increase diminishes at higher normal stresses primarily attributable to more severe asperity wear. These findings highlight the importance of slip velocity in controlling the transient evolution of aperture and permeability of a rock fracture. Our study also provides constraints on the constitutive parameters in the combined aperture model for describing transient shear-induced fracture dilatancy. We suggest that it is crucial to incorporate the velocity-dependent aperture model to simulate the nonlinear evolution of fracture aperture in future analytical and numerical models involving coupled hydromechanical processes in geoenergy systems.

Key words: Fracture and flow; Permeability and porosity; Fractures, faults, and high strain deformation zones.

1 INTRODUCTION

The hydromechanical behaviour of faults and fractures in natural rocks are essential for various geological and engineering activities, including natural earthquakes (Sibson 1985; Rudnicki & Chen 1988), groundwater flow (Zhou *et al.* 2023), energy exploitation (Das & Zoback 2013), radioactive waste disposal (Orellana *et al.* 2019), gas storage (Vilarrasa & Carrera 2015), etc. A fundamental mechanism that controls the behaviour of rock fractures is shear-induced dilatancy (Barton *et al.* 1985; Elsworth & Goodman 1986; Ishibashi *et al.* 2016), which elucidates the proclivity of a fracture to widen under shear loading. In particular, shear-induced dilatancy of fractures due to fluid injection plays a key role in the permeability enhancement in unconventional reservoirs (McClure & Horne 2014; Ye & Ghassemi 2018). Fluid injection into the subsurface associated with the hydraulic stimulation of unconventional reservoirs, including shale gas reservoirs (Das & Zoback 2013; Kim & Moridis 2015) and hot-dry-rock reservoirs (Murphy *et al.* 1978; Olasolo *et al.* 2016; Schoenball *et al.* 2020), is currently prevalent for increasing reservoir permeability to improve the recovery of geoenergy. However, it is also known to potentially induce seismic hazard by reactivating fractures and faults, posing a major challenge

to these subsurface injection activities (Zang *et al.* 2014; Keranen & Weingarten 2018; Kim *et al.* 2018; Schultz *et al.* 2020; Ji *et al.* 2022a). For example, the hydraulic stimulation of low-permeability hot-dry-rock reservoirs has caused the M_L (local magnitude) 3.4 earthquake in Basel, Switzerland (Häring *et al.* 2008), the M_L 2.9 earthquake in Soultz-sous-Fôrets, France (Baisch *et al.* 2010) and the M_w (moment magnitude) 5.4 earthquake in Pohang, South Korea (Kim *et al.* 2018). Similarly, hydraulic fracturing in shale gas reservoirs has triggered the M_L 5.7 and M_L 5.3 earthquakes in the south Sichuan basin, China (Lei *et al.* 2019) and the M_w 3.9 earthquake in western Canada (Bao & Eaton 2016).

Transient dilatancy of rock fractures in low-permeability reservoirs associated with slip is key to the success of permeability enhancement in geoenergy systems (Willis-Richards *et al.* 1996; Ye & Ghassemi 2018; Hu *et al.* 2020; Fu *et al.* 2021). Moreover, if the dilation rate of the fracture exceeds the rate of fluid influx, the pore fluid in the fracture will be depressurized (Brace & Martin 1968; Brantut 2020), leading to an increased effective normal stress and thereby enhanced shear strength of the fracture, known as dilatant strengthening (Rice 1975; Sleep 2006; Samuelson *et al.* 2009, 2011). This is likely to inhibit fault slip through the prevention of earthquake nucleation (Rudnicki & Chen 1988) and rupture propagation (Sibson 1985), thus mitigating the seismic hazard (Scholz 1988; Segall *et al.* 2010; Cappa *et al.* 2018; Aben & Brantut 2021). Particularly in the case of injection-induced seismicity, transient dilation could induce pore pressure drops on a fault segment and the stress perturbation on the adjacent fault segment is thus mitigated, potentially reducing the risk of dynamic rupture (*eg.* Cappa *et al.* 2018; Ciardo & Lecampion 2019; Zhang *et al.* 2019a; Brantut 2020). Therefore, it is of particular importance to study the transient fracture dilation accompanying fracture slip.

The fracture aperture is known to change during slip due to the re-arrangement and destruction of asperities (Elsworth & Goodman 1986; Fang *et al.* 2017). When slip occurs on a fracture, the aperture could increase as a result of dilation (Barton *et al.* 1985; Ishibashi *et al.* 2016) or decrease due to compaction (Morrow & Byerlee 1989; Niemeijer & Spiers 2007; Fang *et al.* 2017). In most cases, especially in brittle rocks, the apertures of initially bare fractures tend to increase with fracture slip even at high normal stresses (Barton *et al.* 1985; Esaki *et al.* 1999; Ye & Ghassemi 2018). The displacement-dependent increase of fracture aperture (Δb) can be quantitatively described by the increase of slip displacement (Δu) and dilation angle (ω) as (Barton *et al.* 1985),

$$\Delta b = \Delta u \cdot \tan\omega \tag{1}$$

In addition to the slip displacement, the slip velocity (v) also influences the transient evolution of a fracture aperture during slip (Segall & Rice 1995; Samuelson *et al.* 2009; Fang *et al.* 2017; Ji *et al.* 2023). Particularly, when subject to a velocity change from v_{i-1} to v_i, the transient evolution of incremental porosity ($\Delta\varepsilon$) of the gouge layer in a gouge-filled fracture can be expressed as (Segall & Rice 1995; Sleep 1995; Samuelson *et al.* 2009; Rudnicki 2022),

$$\Delta\varepsilon = \varepsilon_i - \varepsilon_{i-1} = -\psi \cdot \ln\left[\frac{v_{i-1}}{v_i}\left(1 + \left(\frac{v_i}{v_{i-1}} - 1\right)\cdot e^{-v_i \cdot t_i / D_c}\right)\right], \tag{2}$$

where Ψ is the dilation factor scaling the magnitude of dilation in response to the velocity step; i refers to the ith velocity step; ε is the porosity of gouge layer; t_i is the time since the ith velocity step; D_c is the characteristic slip distance over which the frictional contacts are renewed (Dieterich 1979; Ruina 1983). The change in porosity in eq. (2) is associated with the thickness change of the gouge layer and could be described as $\Delta\varepsilon \cong \Delta H/H$, where ΔH and H are the velocity-induced thickness change and the thickness before the velocity change, respectively (Samuelson *et al.* 2009). For initially bare rock fractures, $\Delta\varepsilon$ could be interpreted as the ratio between the velocity-induced aperture change and the aperture before the velocity change. Thus, the transient aperture of an initially bare fracture influenced by the velocity change (b_{evo}) can be expressed as (Fang *et al.* 2017),

$$b_{evo} = b \cdot (1 + \Delta\varepsilon_i). \tag{3}$$

where b is the fracture aperture uncorrected by the velocity change at the ith velocity step. The fracture aperture is commonly linked to permeability by $k = b^2/12$ (Snow 1969; Witherspoon et al. 1980).

The dilation angle (ω) of initially bare fractures in the displacement-dependent aperture model (eq. 1) has been extensively studied (Melin 2012) and is normally in the range of 0–30°. It tends to increase with increasing fracture roughness and decreasing normal stress (Barton & Choubey 1977). The dilation factor (Ψ in eq. 2) of gouge layers was measured ranging from 10^{-5} to 10^{-3} by Samuelson *et al.* (2009) and Ashman & Faulkner (2023). In a numerical study on dilatancy and friction of gouge-filled fractures, the variation in the dilation factor (Ψ) in such ranges could result in significant changes in the drainage state of fractures, affecting the slip stability (Samuelson *et al.* 2011). More recently, the velocity-dependent porosity model has also been applied in a large-scale permeable fault to investigate the impact of porosity and permeability evolution on aseismic slip induced by fluid injection (Yang & Dunham 2021). However, for initially bare fractures, the dilation factor (Ψ) and characteristic slip distance (D_c) in the velocity-dependent aperture model (eq. 2) are still poorly constrained, restricting the incorporation of this important semi-analytical model into the analytical and numerical analysis of fracture permeability and stability.

To constrain the constitutive parameters in the displacement- and velocity-dependent aperture models, we performed numerical inversions based on the experimental data collected from 16 sets of normal stress unloading tests on sandstone samples (Yin *et al.* 2023) to obtain the model parameters and explore their dependence on surface roughness and normal stress. This suite of experimental results allowed us to investigate the temporal evolution of shear-induced dilatancy of rock fractures comprehensively.

2 MATERIALS AND METHODS

2.1 Sample preparation and experimental method

Fracture surfaces with an xy plane projection area of 100 × 200 mm and different joint roughness coefficient (JRC, Barton *et al.* 1985) values of 3.21, 5.62, 7.36 and 12.16 were prepared and tested in this study. A 3-D laser scanner with an accuracy of ±10 μm was utilized to measure the 3-D coordinates of the surface morphology (Fig. 1), which were used to calculate the surface roughness parameter Z_2 as (Tse & Cruden 1979),

$$Z_2 = \left[\frac{1}{M}\sum_{i=1}^{M}\left(\frac{z_{i-1} - z_i}{y_{i-1} - y_i}\right)^2\right]^{\frac{1}{2}}, \tag{4}$$

where y_i and z_i are the coordinates of a 2-D fracture profile along the shear direction (*ie.* y-direction in Figs 1a–d); M represents the number of sampling points distributed along the profile at a constant interval of 1 mm. Fifty profiles along the shear direction with an equal interval of 2 mm were used to obtain the average Z_2 value of each fracture surface (Yin *et al.* 2023). The average JRC value was

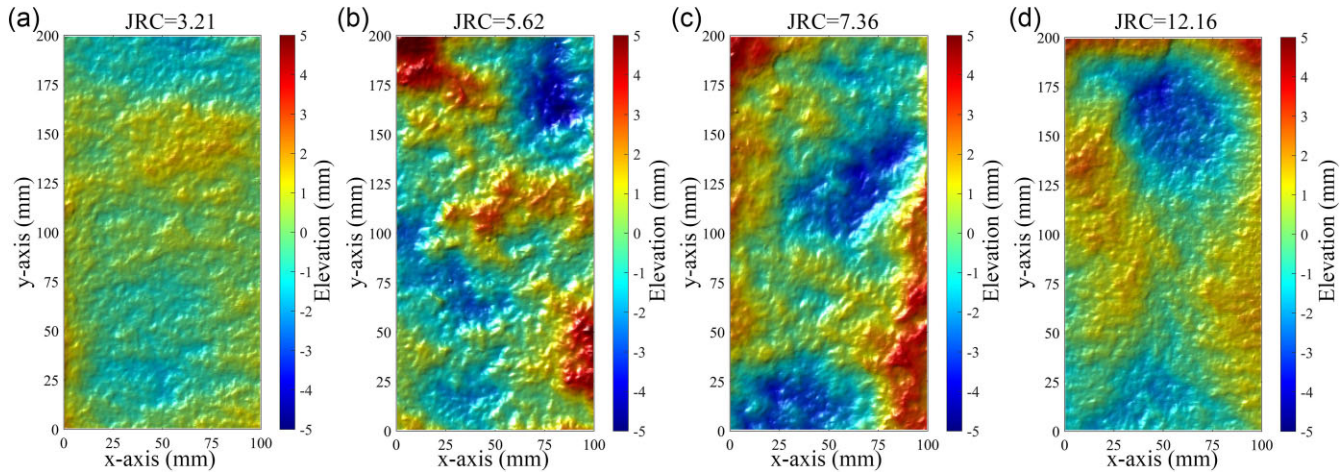

Figure 1. Fracture surface topography. Fractures with different values of JRC were used in this study, that is, (a) JRC = 3.21, (b) JRC = 5.62, (c) JRC = 7.36 and (d) JRC = 12.16.

then calculated based on the empirical correlation between JRC and Z_2 as (Tse & Cruden 1979),

$$\mathrm{JRC} = 32.2 + 32.47\log_{10} Z_2. \tag{5}$$

Using the 3-D scanning data as a reference, precise surface engraving was performed on sandstones at a bit rate of 18 000 r min^{-1} to prepare the samples employed in this study. The raw sandstone materials with a density of 2.71 g cm^{-3} and a uniaxial compressive strength (UCS) of 49.88 MPa were collected from Wuding County, Yunnan Province, China. Four replicas were made for each fracture and thus a total of 16 sandstone samples were prepared for the normal stress unloading tests (Yin *et al.* 2023) to investigate the dilation of rock fractures induced by slip under the conditions of unloading normal stress (e.g. landslide, tunnel excavation and injection-induced seismicity).

The tests were performed on the MIS-233–1-55–03 servo-controlled direct shear apparatus at Nagasaki University (Fig. 2, Jiang *et al.* 2004; Yin *et al.* 2023). Two digital load cells were placed on the top of the upper shear box to measure the normal load and one digital load cell was connected to the side of the shear box to measure the shear load (Jiang *et al.* 2004). Five linear variable differential transformers (LVDTs), each possessing a precision of 0.001 mm, were employed for the measurement of displacements. One LVDT was affixed on the lower shear box for the purpose of quantifying the slip displacement, while the remaining four LVDTs were positioned at the four corners of the upper shear box to monitor the normal displacement. The data acquisition and instrumentation systems used in this study were based on LabVIEW (Han *et al.* 2020). The acquisition system recorded the normal stress and shear stress at a sampling frequency of 1 Hz, each achieving a precision of 0.001 MPa. In parallel, the acquisition system captured the slip and normal displacements at a sampling rate of 1 Hz, each with an accuracy of 0.001 mm. The increase of normal displacement indicates the compression of the fracture whereas the reduction of normal displacement implies the dilation of the fracture. The positive change of the slip displacement is associated with the activation of the fracture. The slip velocity was computed as the difference between adjacent slip displacements divided by the time interval of the acquisition (1 s). The experimental conditions for all the 16 samples are listed in Table 1. Note that five normal stress unloading tests were conducted repeatedly under each experimental condition but we focused only on the first test to evaluate the roles of surface roughness and normal stress. A more detailed description for the 16 normal stress unloading tests has been reported by Yin *et al.* (2023).

Before each test, the sample was positioned within the shear box, and an initial normal stress (σ_n^0) was applied at a loading rate of 0.5 MPa min^{-1} until reaching the target value. Note that for each JRC, four different initial normal stresses, that is, 1, 3, 5 and 7 MPa, were tested (see Fig. A1 for all testing results). Subsequently, in each test (Fig. 3), the whole experimental process can be divided into three stages, consisting of a displacement-driven shear stage (stage I), a shear stress adjustment stage (stage II) and an unloading-driven shear stage (stage III). During the displacement-driven shear stage, the normal stress remained constant, while the lower shear box was actuated by the horizontal jack at a loading rate of 0.3 mm min^{-1} to apply shear stress (τ) until reaching the peak shear stress ($\tau_{\max}$). Then, during the shear stress adjustment stage, τ was linearly reduced to 85% of $\tau_{\max}$ at a rate of 1 MPa min^{-1} and held constant afterwards at an always constant σ_n^0. Finally, during the unloading-driven shear stage, we unloaded the normal stress at a rate of 0.6 MPa min^{-1} to induce fracture opening and slip. We further divided the unloading-driven shear stage into four segments, including a pre-slip segment during which the fracture dilated because of normal stress unloading but slip did not occur, a velocity-fluctuation segment where the fracture exhibited dynamic slip events with fluctuating slip velocities, an accelerating slip segment with constant shear stress where the fracture showed dramatically increasing slip displacement, and an accelerating slip segment with decreasing shear stress where the apparatus could not provide constant shear stress as a result of the high slip velocity.

2.2 Numerical inversion using the combined aperture model

The modelled fracture aperture considering both displacement- and velocity-dependent aperture changes can be expressed as (Ji *et al.* 2023),

$$b_{\mathrm{evo}}^n = b_{\mathrm{slip}}^n \prod_{i=0}^{i=\mathrm{n}} (1 + \Delta\varepsilon_i), \tag{6}$$

where the indices n and i refer to the nth and ith velocity steps, respectively ($i \leq n$); b_{evo} is the aperture predicted by the combined displacement- and velocity-dependent aperture model; b_{slip} is the

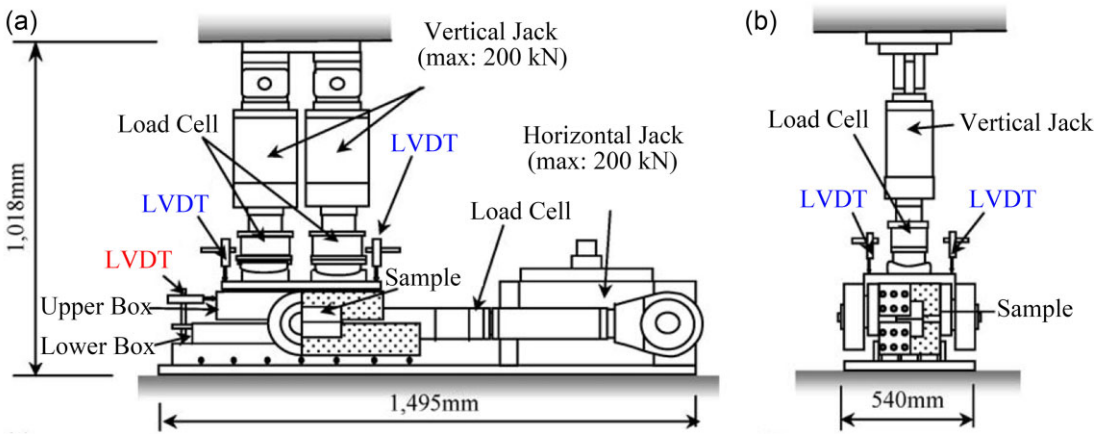

Figure 2. Schematic of the MIS-233–1-55–03 servo-controlled direct shear testing apparatus at Nagasaki University (modified after Jiang *et al.* 2004). (a) Side view and (b) front view. One LVDT is installed on the lower shear box to measure the slip displacement, and four LVDTs are placed on top of the upper shear box to measure the normal displacement. Two load cells are placed on top of the upper shear box to measure the normal load and one load cell is connected to the side of the shear box to measure the shear load.

Table 1. Fracture properties, experimental conditions and best-fitting parameters in the combined displacement- and velocity-dependent aperture model

Test	Natural mechanical aperture (b_{max}) (mm)	JRC[a]	Initial normal stress (σ_n^0) (MPa)	Dilation factor (ψ)	Characteristic slip distance (D_c) (mm)	Dilation angle (ω) (°)	RMSE (mm)[b]	Convergence[c]
1–1	0.7492	3.21	1	0.1414	2.0000	2.8446	0.0022	×
1–2	0.7492	3.21	3	0.2118	1.6763	3.2698	0.0039	√
1–3	0.7492	3.21	5	0.0004	0.0042	4.1171	0.0034	√
1–4	0.7492	3.21	7	0.0117	0.2077	3.9374	0.0064	√
2–1	1.6800	5.62	1	0.0559	0.7572	1.4060	0.0051	√
2–2	1.6800	5.62	3	0.0201	0.5820	0.5526	0.0049	√
2–3	1.6800	5.62	5	0.0020	0.0613	3.6879	0.0047	√
2–4	1.6800	5.62	7	0.0041	0.1092	3.9177	0.0020	√
3–1	1.7299	7.36	1	0.0205	2.0000	6.5125	0.0075	×
3–2	1.7299	7.36	3	0.0116	0.5080	4.6682	0.0068	√
3–3	1.7299	7.36	5	0.0093	0.0882	7.3763	0.0073	√
3–4	1.7299	7.36	7	0.0138	2.0000	10.7398	0.0074	×
4–1	1.3405	12.16	1	0.0111	0.1950	12.8096	0.0048	√
4–2	1.3405	12.16	3	0.0177	0.0216	12.9258	0.0101	√
4–3	1.3405	12.16	5	0.0053	0.3060	10.3144	0.0078	√
4–4	1.3405	12.16	7	0.0051	0.1176	6.3719	0.0086	√

[a]JRC refers to the Joint Roughness Coefficient (Barton *et al.* 1985).
[b]RMSE is the root mean square error between the predicted and measured mechanical apertures.
[c] × means the optimization for the non-convergent inversions and √ means the optimization for the convergent inversions.

aperture computed as the displacement-dependent aperture change (eq. 1) plus the aperture at the onset of stable sliding and $\Delta\varepsilon$ is the incremental porosity/aperture in eqs (2) and (3) (particularly, $\Delta\varepsilon_0$=0). When computing $\Delta\varepsilon_i$, t_i in eq. (2) is calculated as,

$$t_i = \frac{u_n^{\text{end}} - u_i^{\text{ini}}}{v_i}, \tag{7}$$

where u_n^{end} is the slip displacement at the end of the nth velocity step; u_i^{ini} is the slip displacement at the start of the ith velocity step and v_i is the slip velocity during the ith velocity step.

As the model was derived from velocity-stepping shear tests showing stable sliding at low velocities (Samuelson *et al.* 2009), the velocity-fluctuation segment characterized by abrupt slip velocity changes was excluded from our study. The accelerating slip segment with decreasing shear stress has also been excluded as the constant shear stress boundary condition cannot be maintained in this segment. As the normal stress change of the 16 normal stress unloading tests is less than 5 MPa, the normal displacement change induced by normal stress unloading could be assumed as linearly related to the normal stress change (Rutqvist *et al.* 2008; Ji *et al.* 2022b). This relationship is fitted based on the measured changes of normal displacement and normal stress during the pre-slip segment in each test to estimate the combined normal stiffness of the shear box, rock matrix and fracture. The near linear relationship between the normal stress change and normal displacement change confirms that the normal deformation caused by normal stress unloading is mostly elastic (Fig. 4). The slopes of the fitted lines were taken as the combined normal stiffnesses (k_n). In addition, note that we assumed a constant dilation angle (eq. 1) in our model as the slip displacement before the accelerating slip segment

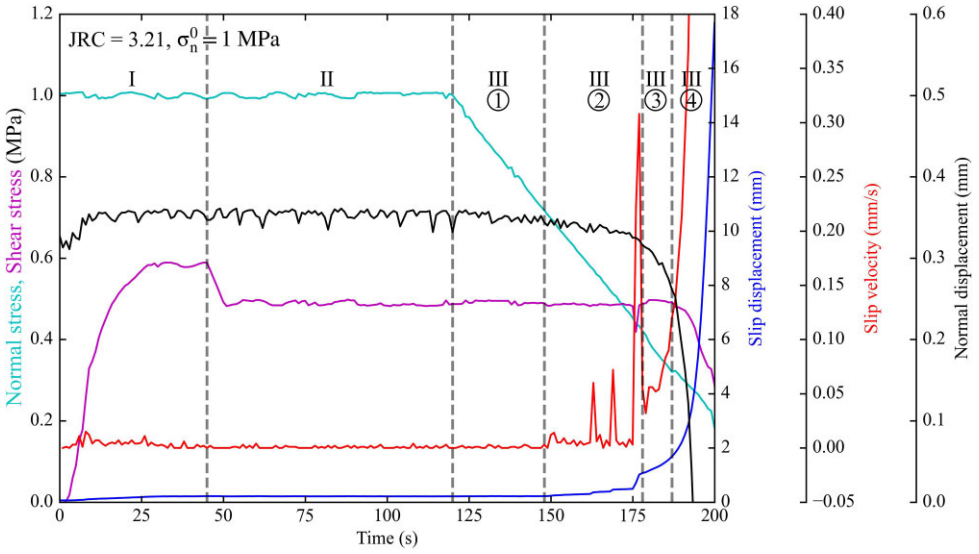

Figure 3. Time history of normal stress, shear stress, slip displacement, slip velocity and normal displacement of test 1–1 conducted on the fracture surface with JRC = 3.21 at an initial normal stress (σ_n^0) of 1 MPa. Positive changes in normal displacement indicate normal compaction of the fracture. The grey dashed lines divide the test into three stages, consisting of (I) a displacement-driven shear stage, (II) a shear stress adjustment stage and (III) an unloading-driven shear stage. The unloading-driven shear stage is further divided into four segments, including ① a pre-slip segment, ② a velocity-fluctuation segment, ③ an accelerating slip segment with constant shear stress and ④ an accelerating slip segment with decreasing shear stress. The ratio of changes in normal stress and normal displacement in the pre-slip segment was used to estimate the combined normal stiffness of the shear box, rock matrix and fracture. The slip displacement, slip velocity and normal displacement in the accelerating slip segment with constant shear stress were used to constrain the parameters in the displacement- and velocity-dependent aperture model. Note that the peak slip velocities may be underestimated from the data sampled at 1 Hz (*cf.* Ohnaka & Shen 1999), but the underestimation may not impact our numerical inversion in which the maximum slip velocity is as low as 0.373 mm s^{-1}.

with decreasing shear stress in all the 16 tests is not more than 2 mm.

To investigate the transient shear-induced dilatancy, we focused on the aperture change caused only by shear dilation and subtracted the deformations of shear box, rock matrix and fracture opening induced by normal stress unloading from the measured mechanical aperture in the accelerating slip segment with constant shear stress. The vertical LVDTs can only measure the average aperture change, and the maximum mechanical aperture without any external load (b_{max} in Table 1) in this study was estimated as the root mean square (RMS) asperity height of the fracture (Fang *et al.* 2017; Magsipoc *et al.* 2020). Given the substantially greater capacity for normal deformation of the interstitial gap between adjacent fracture walls compared to that of the shear box and rock matrix, we consider that the normal deformation monitored by the LVDTs is predominantly attributable to the change in the fracture aperture. The mechanical aperture at the onset of each test (b_{ini}) could thus be estimated as,

$$b_{ini} = b_{max} - \frac{\sigma_n^0}{k_n}, \tag{8}$$

where σ_n^0 is the initial normal stress. The measured mechanical aperture (b_{exp}) during the test can then be computed as,

$$b_{exp} = b_{ini} - (h - h_0) \tag{9}$$

where h stands for the measured normal displacement during the test; h_0 refers to the measured normal displacement when the test starts. After the reactivation of the preexisting fracture, the measured mechanical aperture excluding the normal deformation induced by normal stress unloading but including the shear dilation by slip (b_{exp}^{slip}) could be calculated with the following equation,

$$b_{exp}^{slip} = b_{exp} + \frac{\sigma_n - \sigma_n^{slip,0}}{k_n}, \tag{10}$$

where σ_n is the normal stress after fracture reactivation and $\sigma_n^{slip,0}$ is the normal stress at the onset of fracture reactivation.

After the computation of the measured mechanical aperture change induced by shear dilation, we conducted numerical inversions based on the data collected from the 16 sets of normal stress unloading tests to constrain the model parameters in the combined aperture model and explore their dependences on surface roughness and normal stress. Particularly, we optimized the parameters in the model described by eqs (1)–(2) and eqs (6)–(7) to match the mechanical aperture predicted by the model (b_{evo}) with the measured mechanical aperture (b_{exp}^{slip}) by searching the minimum root mean square error (RMSE) between the mechanical apertures measured in the experiments and predicted by the combined aperture model. That is, the following objective function has been minimized during the optimization,

$$F_{obj} = \sqrt{\frac{1}{n}\sum_{i=1}^{n}\left(b_{evo}^{i} - b_{exp}^{slip,i}\right)^2}, \tag{11}$$

where F_{obj}, that is, RMSE, is the objective function to be minimized; b_{evo}^{i} is the mechanical aperture predicted by the model at the ith velocity step; $b_{exp}^{slip,i}$ is the measured mechanical aperture at the ith velocity step and n is the total number of data points. There were three independent parameters (i.e. Ψ, D_c and ω) that need to be constrained during the optimization and thus three degrees of freedom were in the numerical inversions. The genetic algorithm (GA, Holland 1992; Zbigniew 1996) was utilized to find the global minimum of F_{obj} over the ranges of $0 \le \Psi \le 0.5$, $10^{-5} \le D_c \le 2$ mm and $0 \le \omega \le 20^{\circ}$ for all the numerical inversions. The Python package named scikit-opt was used to implement the numerical inversions based on GA (Zhang *et al.* 2023b).

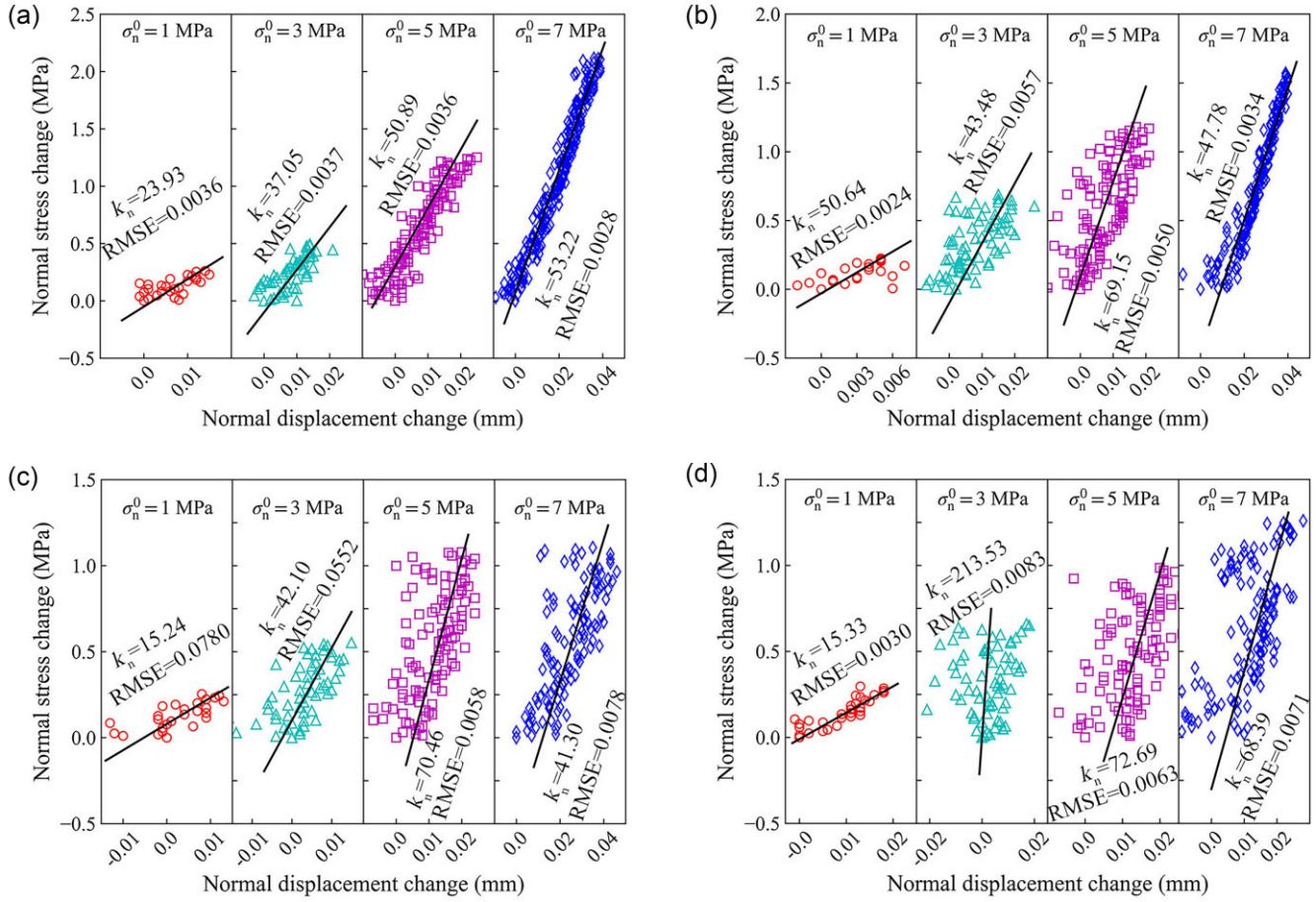

Figure 4. The determination of the combined normal stiffness of the shear box, rock matrix and fracture in the 16 normal stress unloading tests based on changes in normal stress and normal displacement in the pre-slip segment. The combined normal stiffness of the samples with a JRC of (a) 3.21, (b) 5.62, (c) 7.36 and (d) 12.16 under different initial normal stresses (σ_n^0) were determined using linear fit. The scatters are the recorded data of the changes of normal stress and normal displacement in each test. The black solid lines on top of the data are the best-fitted lines. The determined combined normal stiffness (k_n, in MPa mm^{-1}) and the goodness of the fit (quantified by RMSE) are displayed beside the best-fitting lines. Note that the unit of RMSE is mm because normal displacement change was taken as a function of normal stress change when conducting the fit.

3 RESULTS AND DISCUSSION

3.1 Contribution of slip velocity to transient aperture evolution

Fig. 5 presents the evolution of measured (b_{exp}^{slip}), displacement- and velocity-dependent (b_{evo}), and displacement-dependent (b_{slip}) mechanical apertures, velocity factor ($\frac{b_{evo}-b_0}{b_{slip}-b_0}$, where b_0 is the measured aperture at the onset of the accelerating slip segment with constant shear stress), and slip velocity during the accelerating slip segment with constant shear stress used for numerical inversion. The maximum slip displacement change and aperture change are 2.141 mm (in the test with a σ_n^0 of 3 MPa and a JRC of 7.36) and 0.315 mm (in the test with a σ_n^0 of 5 MPa and a JRC of 12.16), respectively. The slip velocity generally increases with slip displacement with upper and lower bounds of 0.001 and 0.373 mm s^{-1}, respectively. The velocity factor characterizes the contribution of slip velocity additional to that of slip displacement to the mechanical aperture change. It is higher than 1 when the slip velocity tends to enhance the modelled aperture increase, while the aperture increase is suppressed by the velocity when it is lower than 1. The velocity factor ranges from −1.95 to 3.66, suggesting a significant contribution of slip velocity to aperture change in the accelerating slip segments with constant shear stress in our experiments. Moreover, the nonlinear evolution of fracture aperture change with evolving slip velocity can only be modelled by combining displacement- and velocity-dependent aperture models. The influence of slip velocity on the nonlinear aperture change could be attributed to the frequent velocity change. Frictional contacts on a fracture would be renewed over a characteristic slip distance after a change in slip velocity (Dieterich 1979; Ruina 1983), causing the fracture aperture to nonlinearly evolve. The velocity changes so frequently that the aperture cannot be stabilized between each two adjacent velocity steps. Consequently, the transient change in the fracture aperture is affected by the temporal evolution of slip velocity.

The four subplots along the horizontal direction represent the evolution of the results with different initial normal stresses (σ_n^0) at the same JRC. With the increase of initial normal stress, the velocity factor under the four JRC values changes from a monotonically increasing trend to a trend showing a reduction followed by an increase, while the slip velocity at the onset of the accelerating slip segment with constant shear stress decreases. This transition may be caused by the wear of asperities under higher normal stresses. Particularly, when the normal stress is low, the deformation of asperities is negligible, and the slip velocity increase could monotonically promote the aperture increase. However, if the normal stress

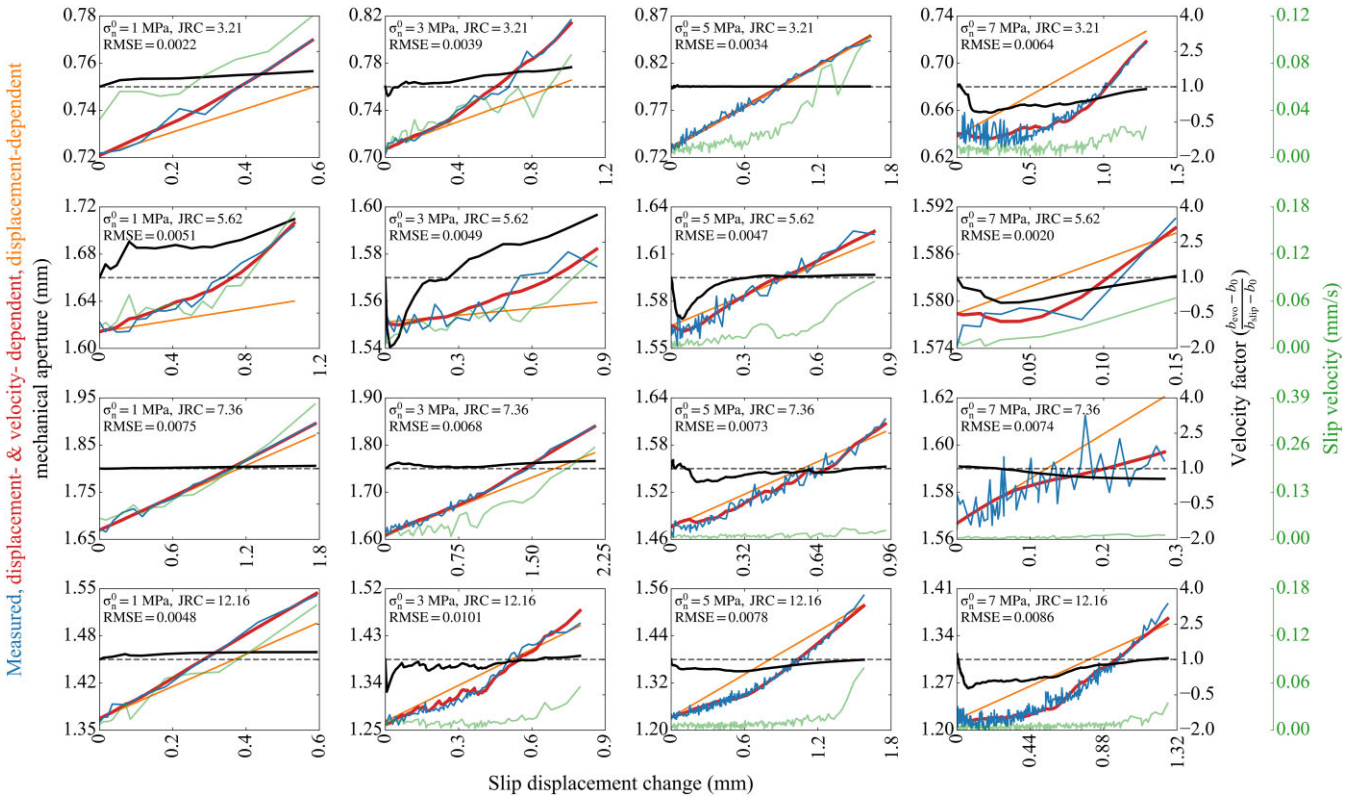

Figure 5. Evolution of mechanical aperture, velocity factor $(\frac{b_{evo}-b_0}{b_{slip}-b_0})$ and slip velocity in the 16 tests conducted on fractures with different JRC at different initial normal stresses (σ_n^0). The slip displacement change is offset to zero at the onset of the accelerating slip segment with constant shear stress. The velocity factor is the ratio between $(b_{evo} - b_0)$ and $(b_{slip} - b_0)$, where b_0 is the measured aperture at the onset of the accelerating slip segment with constant shear stress. With the increase of normal stress, the velocity factor changes from a monotonically increasing trend to a trend showing a reduction followed by an increase. This transition is promoted by higher JRC values. Note that we used different scales except for the velocity factor for better presentation of the results. The grey dashed line indicates the velocity factor with a value of 1.

on the fracture is high enough to cause asperity wearing, the aperture increase could be slightly inhibited firstly and then promoted by further velocity increase. The wearing of the surface asperities in this study has been visually and quantitatively demonstrated by Yin *et al.* (2023), where the ratio of sheared area to the total fracture area was dramatically intensified under high initial normal stresses. One exception to this transition occurs when σ_n^0 is 7 MPa and JRC is 7.36, where the velocity factor decreases monotonically and is always lower than 1. The reason for this exception is probably that the slip displacement change (0.761 mm) and velocity (0.011 mm s^{-1}) at the end of the accelerating slip segment with constant shear stress is not high enough to lead to the increase of the velocity factor.

The four subplots in the same column present the evolution of the results with different JRC values at the same initial normal stress (σ_n^0). With the increase of JRC, the transition of the velocity factor from monotonic increase to a trend showing a reduction followed by an increase is promoted and occurs at lower initial normal stresses, accompanying the generally decreasing velocity at the onset of the accelerating slip segment with constant shear stress. A higher JRC normally indicates a larger maximum asperity height and less real contact area of the asperities on a pair of fracture surfaces (Hisakado 1974; Dieterich & Kilgore 1996), which means the asperities are easier to be worn under the same average normal stress due to the locally concentrated stress on the contacted asperities. As a result, the worn asperities associated with increasing JRC could make the transition earlier and more significant, potentially facilitating the occurrence of such transition at lower normal stresses. This mechanism could be evidenced by the increasing ratio of sheared area to the total fracture area with increasing JRC value of fracture surface, especially at higher normal stresses (Yin *et al.* 2023).

3.2 Constraining constitutive parameters in the transient aperture model

We explored the dependence of the constitutive parameters in the displacement- and velocity-dependent aperture models, including dilation factor (ψ), characteristic slip distance (D_c) and dilation angle (ω), on the initial normal stress and surface roughness. The best-fitting values of these parameters, minimum RMSEs and convergence of all the 16 tests are summarized in Table 1. The convergent inversion means the best-fitting values are unique in the 3-D solution space. On the contrary, the non-convergent inversion means the best-fitting values are not unique in the 3-D solution space. Most numerical inversions (13 out of 16) converged with low RMSEs and thus the optimized parameters are reliable. For the three non-convergent cases (i.e. tests 1–1, 3–1 and 3–4), the RMSE values are comparable with that in the converged cases, suggesting that the optimized parameters for these three tests may also be acceptable to some extent. With initial normal stress variations between 1 and 7 MPa and JRC values between 3.21 to 12.16, ψ of all convergent cases ranges from 0.0004 to 0.2118, D_c from 0.0042 to 1.6763 mm, and ω from 0.55° to 12.93°. The dilation factor of initially bare fractures in sandstone in our study is similar to that reported by Fang *et al.* (2017) on initially bare fractures in shale, Ji

et al. (2023) on initially bare fracture in granite, and Cappa *et al.* (2022) on *in-situ* faults in limestone, while it is 1 to 2 orders of magnitude higher than the dilation factor in synthetic quartz-clay (kaolinite) fault gouge (Ashman & Faulkner 2023) and 2–3 orders of magnitude higher than the dilation factor in fine-grained quartz fault gouge (Samuelson *et al.* 2009). The smaller dilation factor in gouge-filled fractures compared to our initially bare fractures may be due to the pre-compaction/consolidation of gouge before the tests, resulting in its lower sensitivity to velocity. The values of our best-fitting D_c are generally consistent with the D_c reported on initially bare fractures ranging from several micrometres to millimetres (e.g. Marone & Cox 1994; Fang *et al.* 2017; Im *et al.* 2018; Ishibashi *et al.* 2018; Shen *et al.* 2022; Ji *et al.* 2023). The range of dilation angles in our study is similar to that in previous studies, ranging from 0 to 30° (Yeo *et al.* 1998; Chen *et al.* 2000; Melin 2012).

The dilation factor (ψ) decreases and converges with the increase of initial normal stress (σ_n^0) and JRC (Figs 6a and b), indicating that the velocity-dependent dilation can be suppressed by the increase of normal stress and JRC. The convergency and decrease of ψ with σ_n^0 increase in our study is inconsistent with the enigmatic relationship between ψ and σ_n^0 of gouge-filled fractures (Samuelson *et al.* 2009; Ashman & Faulkner 2023), which may be caused by the different responses of initially bare and gouge-filled fractures to normal stress change. Particularly, the increase of normal stress tends to cause the closure of initially bare fractures and thereby inhibit the dilatancy, and ψ is thus decreased. However, the influence of normal stress on gouge-filled fractures may be complicated by the grain packing frameworks (Kohli & Zoback 2013) changing with clay contents (Ashman & Faulkner 2023). In addition, the slight dependency of ψ of gouge-filled fractures on normal stress could be complicated by the development of shear fabrics associated with accumulated shear strain (Logan *et al.* 1992; Samuelson *et al.* 2009). The characteristic slip distance (D_c) decreases with the increase of σ_n^0 (Fig. 6c). Note that, as D_c of the three non-convergent results in Table 1 reaches the upper bound (2 mm), the non-convergent results are neglected when investigating the variation of D_c. D_c also decreases with the increase of JRC (Fig. 6d). The reduction of characteristic slip distance may indicate that the fracture can reach steady state more easily after the change of slip velocity at a higher normal stress and JRC.

Unlike the dilation factor (ψ) and characteristic slip distance (D_c), the dilation angle (ω) does not converge with the variation of neither initial normal stress (σ_n^0) nor JRC. The dilation angle was considered negatively correlated with the effective normal stress within the range of ~2–36 MPa (Barton & Choubey 1977; Chen *et al.* 2000; Kim & Jeon 2019). However, no obvious relationship between the dilation angle and initial normal stress could be observed in our study (Fig. 6e). In addition, the dilation angle is not sensitive to σ_n^0, which may be caused by the limited range of σ_n^0 (from 1 to 7 MPa) and uncertainties in the numerical inversions (indicated by the RMSE values in Table 1 and point sizes in Fig. 6) in our study. Nonetheless, the variation of dilation angle decreases with the increase of σ_n^0. This decrease could be caused by the more severe wear of fracture asperities under higher normal stresses, which could be verified by the increasing ratio of sheared area to the total fracture area with increasing normal stress (Yin *et al.* 2023). The dilation angle generally increases with JRC (Fig. 6f) primarily because of higher asperities, which is consistent with previous experimental results (*cf.* Barton & Choubey 1977; Rafek & Goh 2012). Therefore, under otherwise similar conditions, the displacement dependence is more significant for rougher fractures with higher JRC due to the positive correlation between the dilation angle and displacement-dependent fracture aperture (eq. 1). Furthermore, rougher fracture surfaces tend to experience arrested ruptures due to the significant stress barriers induced by higher asperities (Fryer *et al.* 2022), causing limited slip velocity. The influence of slip velocity on a fracture aperture may be thereby weakened.

3.3 Limitations and suggestions

We constrained the key constitutive parameters, including the dilation angle, dilation factor and characteristic slip distance, in displacement- and velocity-dependent aperture models. Incorporating the role of slip velocity change in controlling the aperture change, in addition to the slip displacement, has successfully replicated the nonlinear evolution of shear-induced aperture changes of fractures. The normal stress applied in our laboratory experiments ranges from 2% to 14% of UCS of the host rock. A much higher normal stress may inhibit both displacement- and velocity-induced aperture increase (Li *et al.* 2022a; Ashman & Faulkner 2023). The fractures with initially bare surfaces in the laboratory here are fresh, dry and tightly matched. It is inferred that weathered and unmated fractures in the field may experience less significant dilation as the dilation factor of gouges is lower than that of initially bare surfaces, primarily depending on the degree of weathering (Barton *et al.* 1985) and the joint matching coefficient (Zhao 1997). In this study, we used a linear displacement-dependent aperture model (*cf.* Barton *et al.* 1985; Cappa *et al.* 2018; Zhang *et al.* 2019a), which is reasonable in relatively small displacement ranges as explored in our experiments. The nonlinear aperture dependency on displacement should be incorporated for large slip displacement cases (*cf.* Fang *et al.* 2017). We assumed the dilation factor, characteristic slip distance and dilation angle as constants in our numerical inversions. These parameters, however, may change with the slip of the fracture (e.g. Marone & Cox 1994). Also note that the aperture here in this study is the mechanical aperture, which is not equivalent to the hydraulic aperture (Chen *et al.* 2000) that was used by Fang *et al.* (2017), Cappa *et al.* (2018) and Ji *et al.* (2023). However, the congruence between alterations in hydraulic aperture and mechanical aperture may remain steadfast in permeable fractures within controlled laboratory settings (Fang *et al.* 2017; Ji *et al.* 2023) and natural field conditions (Cappa *et al.* 2022). Moreover, the results obtained from the accelerating slip segments with constant shear stress in this study, characterized by a slip velocity up to 0.373 mm s^{-1}, cannot extend to the slip regime with extremely high slip velocities, indicating that our results are applicable mostly to slow slipping fractures/fault segments showing no flash heating and associated thermal pressurization (Rice 2006; Tanikawa *et al.* 2010; Acosta *et al.* 2018). Nevertheless, the dilation factor and characteristic slip distance values constrained in this study provide reference magnitudes for inputs in the velocity-dependent aperture model in slow slip regimes.

The characteristic slip distance, dilation angle and dilation factor in this study were constrained in a laboratory setting. Therefore, they should only be reference values in laboratory-scale modelling. For field-scale models, it might be possible to determine the characteristic slip distance using $D_c = \zeta T$, where ζ is a constant estimated as 10^{-2} and T is the thickness of the shear band where shear strain occurs (Marone & Kilgore 1993). The dilation angle could be upscaled base on the experiment results in laboratory. For example, Barton & Bandis (1982) proposed a set of upscaling equations that could link field-scale dilation angles to the JRCs, joint compressive

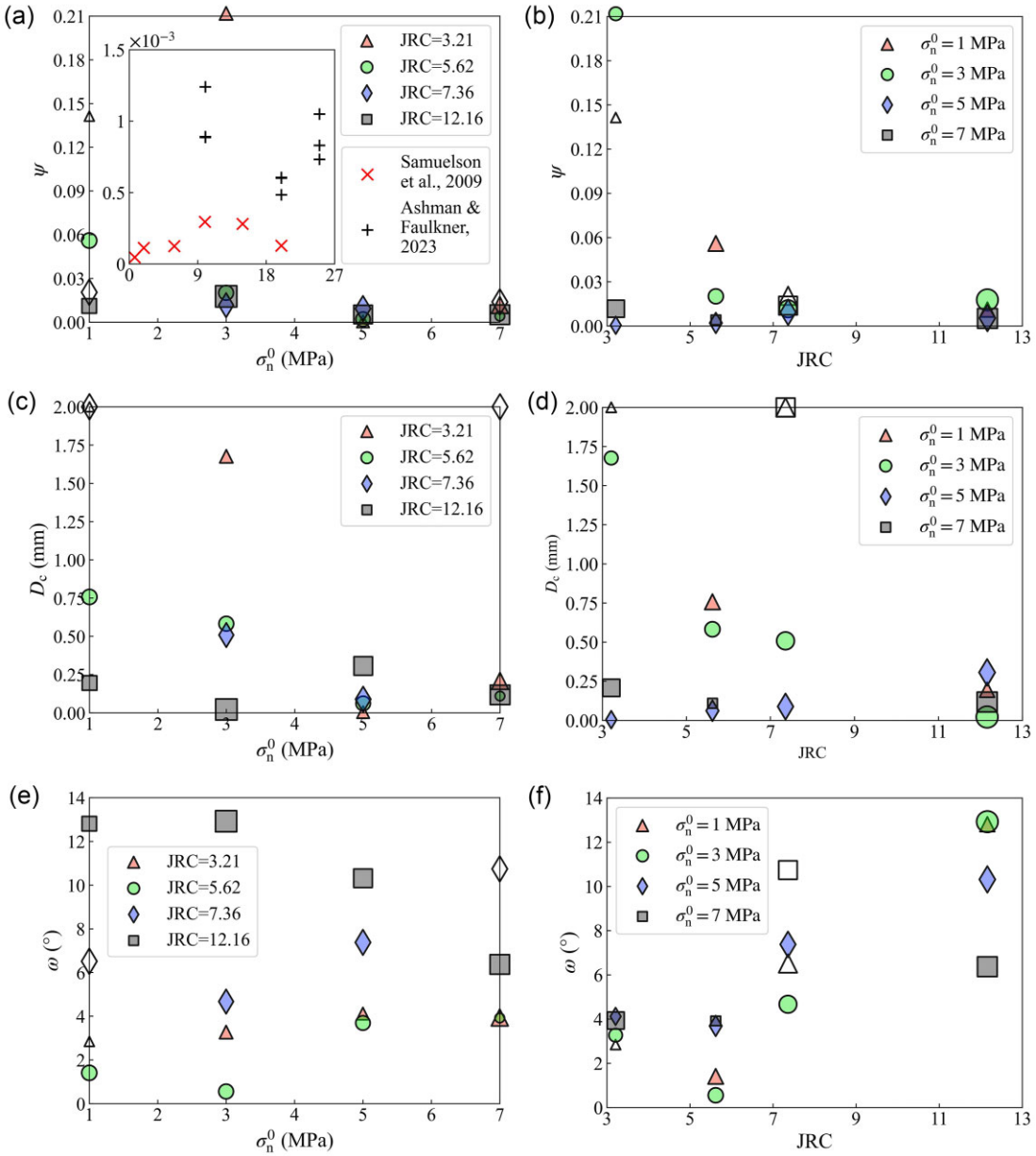

Figure 6. The optimized parameters in the combined displacement- and velocity-dependent aperture model, including (a) and (b) dilation factor (Ψ), (c) and (d) characteristic slip displacement (D_c) and (e) and (f) dilation angle (ω), for the 16 tests conducted on fractures with different JRC values at different initial normal stresses (σ_n^0). The open data points represent the results from the three non-convergent inversions and the solid data points show the converged results. The point sizes are scaled according to the corresponding RMSE values in Table 1 (larger points indicate higher RMSE values). The inset in (a) presents the dilation factors reported by Samuelson *et al.* (2009) and Ashman & Faulkner (2023).

strengths, lengths and effective normal stresses of field-scale fractures. In addition, the dilation factor could be discretely set for each fracture segment in field-scale models to simulate shear-induced dilatancy.

The reproduction of the nonlinear aperture change using the combined displacement- and velocity-dependent aperture model is of great importance for various engineering settings. For instance, in the case of injection-induced fracture reactivation and permeability evolution, the nonlinear aperture evolution may complicate the change of pore pressure, effective normal stress and thereby slip response of the fracture, which could in turn alter the aperture change and pore pressure diffusion by changing the slip displacement and velocity, especially in the rupture nucleation stage (Cappa *et al.* 2018; Ciardo & Lecampion 2019; Yang & Dunham 2021; Heimisson *et al.* 2022). Particularly, even an extremely low dilation factor on the order of 10^{-5} to 10^{-3} can cause drastic nonlinear changes in the pore pressure and shear behaviour of a gouge-filled fracture (Samuelson *et al.* 2011; Rudnicki 2022). Besides, the proper assessments of aperture changes and permeability evolution are important for anticipating and managing the injection-induced seismic hazard (Ishibashi *et al.* 2016; Li *et al.* 2022b). Therefore, it is critical to incorporate the velocity-dependent aperture model in future analytical and numerical models involving hydromechanically coupled processes.

The mechanical aperture in this study is the orientation-independent average aperture, which discounts the anisotropic aperture evolution. However, the permeability anisotropy associated with the development of aperture anisotropy, which may influence the propagation of the seismic front in different directions with respect to the principal shear direction, is ignored in this study and needs to be investigated in the future (Shapiro *et al.* 1997; Ji *et al.* 2022c). Flux-driven particle mobilization accompanied by asperity wearing in injection related activities could also impact the permeability evolution (Candela *et al.* 2014) and thus the clogging and unclogging of particles in worn fractures also necessitates further studies. In addition, in this study we investigated only sandstones. It is thus necessary to further explore the controls of surface roughness and normal stress on fractures in other rock types relevant to geoenergy systems.

4 CONCLUSIONS

We combined displacement- and velocity-dependent aperture models to reproduce the temporal evolution of shear-induced dilatancy of fractures in sandstone based on the experimental data from 16 normal stress unloading tests. Our results suggest the following:

(1) The combined aperture model dependent on both slip displacement and velocity can satisfactorily reproduce the nonlinear aperture evolution during the accelerating slip of fractures induced by normal stress unloading better than the displacement-dependent aperture model.

(2) As the initial normal stress in the 16 tests increases, the velocity-dependent mechanical aperture shifts from monotonic increase to reduction followed by an increase with the enhancement of slip velocity, and this shift is promoted by higher surface roughness. This transition indicates that slip velocity could enhance the aperture increase on smoother fractures at lower normal stresses and higher slip velocities.

(3) Both the dilation factor and characteristic slip distance decrease and converge with the increase of both initial normal stress and JRC, signifying the reduced contribution of slip velocity to transient shear-induced fracture dilatancy at higher initial normal stresses and JRC.

(4) The dilation angle increases with JRC, but this effect becomes less significant at higher initial normal stresses, primarily due to the more severe wear of fracture asperities under higher normal stresses.

The results in this study demonstrate the influence of slip velocity on the shear-induced dilatancy of fractures, which could also provide reference input values for the combined displacement- and velocity-dependent aperture model in future hydromechanical analyses of fracture reactivation and permeability evolution.

ACKNOWLEDGMENTS

This work has been supported by the Helmholtz Association's Initiative and Networking Fund for the Helmholtz Young Investigator Group ARES (contract number VH-NG-1516) and the National Natural Science Foundation of China (no. 42090023). The financial support provided by China Scholarship Council (CSC no. 202204910299) to S. Zhang is also greatly acknowledged. We appreciate the detailed and constructive reviews by the editor Shiqing Xu, Barnaby Fryer and an anonymous reviewer, which helped us to improve the article. The authorship contribution is as follow: Supeng Zhang (Formal analysis [equal], Software [equal], Visualization [equal], Writing – original draft [lead]), Yinlin Ji (Conceptualization [equal], Methodology [equal], Supervision [equal], Writing – original draft [equal], Writing – review & editing [equal]), Hannes Hofmann (Funding acquisition [lead], Supervision [equal], Writing – review & editing [equal]), Qian Yin (Data curation [equal]), Shouding Li (Funding acquisition [equal], Supervision [equal]), Yuanchao Zhang (Data curation [equal]).

CONFLICT OF INTEREST

The authors declare that they have no identifiable conflicting financial interests or personal affiliations that could have conceivably impacted the work presented in this paper.

DATA AVAILABILITY

The experimental data generated in this study is available at https://doi.org/10.6084/m9.figshare.25408543.v1 (Zhang *et al.* 2023a), and the Python code for the numerical inversion is freely available via https://doi.org/10.6084/m9.figshare.23995719.v1 (Zhang *et al.* 2023b).

REFERENCES

Aben, F.M. & Brantut, N., 2021. Dilatancy stabilises shear failure in rock. *Earth planet. Sci. Lett.,* **574,** 117174. doi:10.1016/j.epsl.2021.117174.

Acosta, M., Passelègue, F.X., Schubnel, A. & Violay, M., 2018. Dynamic weakening during earthquakes controlled by fluid thermodynamics. *Nat. Commun.,* **9**(1), 3074.

Ashman, I.R. & Faulkner, D.R., 2023. The effect of clay content on the dilatancy and frictional properties of fault gouge. *J. geophys. Res.: Solid Earth,* **128**(4), e2022JB025878.

Baisch, S., Vörös, R., Rothert, E., Stang, H., Jung, R. & Schellschmidt, R., 2010. A numerical model for fluid injection induced seismicity at Soultz-sous-Forêts. *Int. J. Rock Mech. Min. Sci.,* **47**(3), 405–413.

Bao, X. & Eaton, D.W., 2016. Fault activation by hydraulic fracturing in western Canada. *Science,* **354**(6318), 1406–1409.

Barton, N. & & Bandis,, S., 1982. Effects of block size on the shear behavior of jointed rock, p. ARMA–82-739, Presented at the The 23rd U.S Symposium on Rock Mechanics (USRMS). Berkeley, California.

Barton, N. & Choubey, V., 1977. The shear strength of rock joints in theory and practice. *Rock Mech.,* **10**(1), 1–54.

Barton, N., Bandis, S. & Bakhtar, K., 1985. Strength, deformation and conductivity coupling of rock joints. *Int. J. Rock Mech. Min. Sci. Geomech. Abstr.,* **22**(3), 121–140.

Brace, W.F. & Martin, R.J., 1968. A test of the law of effective stress for crystalline rocks of low porosity. *Int. J. Rock Mech. Min. Sci. Geomech. Abstr.,* **5**(5), 415–426.

Brantut, N., 2020. Dilatancy-induced fluid pressure drop during dynamic rupture: direct experimental evidence and consequences for earthquake dynamics. *Earth planet. Sci. Lett.,* **538,** 116179, doi:10.1016/j.epsl.2020.116179.

Candela, T., Brodsky, E.E., Marone, C. & Elsworth, D., 2014. Laboratory evidence for particle mobilization as a mechanism for permeability enhancement via dynamic stressing. *Earth planet. Sci. Lett.,* **392,** 279–291.

Cappa, F., Guglielmi, Y. & De Barros, L., 2022. Transient evolution of permeability and friction in a slowly slipping fault activated by fluid pressurization. *Nat. Commun.,* **13**(1), 3039, doi:10.1038/s41467-022-30798-3.

Cappa, F., Guglielmi, Y., Nussbaum, C. & Birkholzer, J., 2018. On the relationship between fault permeability increases, induced stress perturbation, and the growth of aseismic slip during fluid injection. *Geophys. Res. Lett.,* **45**(20), doi:10.1029/2018GL080233

Chen, Z., Narayan, S.P., Yang, Z. & Rahman, S.S., 2000. An experimental investigation of hydraulic behaviour of fractures and joints in granitic rock. *Int. J. Rock Mech. Min. Sci.,* **37**(7), 1061–1071.

Ciardo, F. & Lecampion, B., 2019. Effect of dilatancy on the transition from aseismic to seismic slip due to fluid injection in a fault. *J. geophys. Res.: Solid Earth,* **124**(4), 3724–3743.

Das, I. & Zoback, M.D., 2013. Long-period, long-duration seismic events during hydraulic stimulation of shale and tight-gas reservoirs—Part 1: waveform characteristics. *Geophysics,* **78**(6), KS107–KS118.

Dieterich, J.H. & Kilgore, B.D., 1996. Imaging surface contacts: power law contact distributions and contact stresses in quartz, calcite, glass and acrylic plastic. *Tectonophysics,* **256**(1), 219–239.

Dieterich, J.H., 1979. Modeling of rock friction: 1. Experimental results and constitutive equations. *J. geophys. Res.: Solid Earth,* **84**(B5), 2161–2168.

Elsworth, D. & Goodman, R.E., 1986. Characterization of rock fissure hydraulic conductivity using idealized wall roughness profiles. *Int. J. Rock Mech. Min. Sci. Geomech. Abstr.,* **23**(3), 233–243.

Esaki, T., Du, S., Mitani, Y., Ikusada, K. & Jing, L., 1999. Development of a shear-flow test apparatus and determination of coupled properties for a single rock joint. *Int. J. Rock Mech. Min. Sci.,* **36**(5), 641–650.

Fang, Y., Elsworth, D., Wang, C., Ishibashi, T. & Fitts, J.P., 2017. Frictional stability-permeability relationships for fractures in shales. *J. geophys. Res.: Solid Earth,* **122**(3), 1760–1776.

Fryer, B., Giorgetti, C., Passelègue, F., Momeni, S., Lecampion, B. & Violay, M., 2022. The influence of roughness on experimental fault mechanical behavior and associated microseismicity. *J. geophys. Res.: Solid Earth,* **127**(8), e2022JB025113, doi:10.1029/2022JB025113.

Fu, P. *et al.*, 2021. Close observation of hydraulic fracturing at EGS Collab Experiment 1: fracture trajectory, microseismic interpretations, and the role of natural fractures. *J. geophys. Res.: Solid Earth,* **126**(7), e2020JB020840, doi:10.1029/2020JB020840.

Han, G., Jing, H., Jiang, Y., Liu, R. & Wu, J., 2020. Effect of cyclic loading on the shear behaviours of both unfilled and infilled rough rock joints under constant normal stiffness conditions. *Rock Mech. Rock Eng.,* **53**(1), 31–57.

Häring, M.O., Schanz, U., Ladner, F. & Dyer, B.C., 2008. Characterisation of the Basel 1 enhanced geothermal system. *Geothermics,* **37**(5), 469–495.

Heimisson, E.R., Liu, S., Lapusta, N. & Rudnicki, J., 2022. A spectral boundary-integral method for faults and fractures in a poroelastic solid: simulations of a rate-and-state fault with dilatancy, compaction, and fluid injection. *J. geophys. Res.: Solid Earth,* **127**(9), e2022JB024185, doi:10.1029/2022JB024185.

Hisakado, T., 1974. Effect of surface roughness on contact between solid surfaces. *Wear,* **28**(2), 217–234.

Holland, J.H., 1992. *Adaptation in Natural and Artificial Systems: An Introductory Analysis with Applications to Biology, Control, and Artificial Intelligence*. MIT Press.

Hu, L., Ghassemi, A., Pritchett, J. & Garg, S., 2020. Characterization of laboratory-scale hydraulic fracturing for EGS. *Geothermics,* **83,** 101706, doi:10.1016/j.geothermics.2019.07.004.

Im, K., Elsworth, D. & Fang, Y., 2018. The influence of preslip sealing on the permeability evolution of fractures and faults. *Geophys. Res. Lett.,* **45**(1), 166–175.

Ishibashi, T., Elsworth, D., Fang, Y., Riviere, J., Madara, B., Asanuma, H., Watanabe, N. & Marone, C., 2018. Friction-stability-permeability evolution of a fracture in granite. *Water Resour. Res.,* **54**(12), 9901–9918.

Ishibashi, T., Watanabe, N., Asanuma, H. & Tsuchiya, N., 2016. Linking microearthquakes to fracture permeability change: the role of surface roughness. *Geophys. Res. Lett.,* **43**(14), 7486–7493.

Ji, Y., Hofmann, H., Duan, K. & Zang, A., 2022a. Laboratory experiments on fault behavior towards better understanding of injection-induced seismicity in geoenergy systems. *Earth Sci. Rev.,* **226,** 103916, doi:10.1016/j.earscirev.2021.103916.

Ji, Y., Kluge, C., Hofmann, H. & Blöcher, G., 2022b. Effects of external temperature and dead volume on laboratory measurements of pore pressure and injected volume in a rock fracture. *J. Rock Mech. Geotech. Eng.,* **14**(5), 1461–1469.

Ji, Y., Zhang, W., Hofmann, H., Cappa, F. & Zhang, S., 2023. Fracture permeability enhancement during fluid injection modulated by pressurization rate and surface asperities. *Geophys. Res. Lett.,* **50,** e2023GL104662, doi:10.1029/2023GL104662.

Ji, Y., Zhang, W., Hofmann, H., Chen, Y., Kluge, C., Zang, A. & Zimmermann, G., 2022c. Modelling of fluid pressure migration in a pressure sensitive fault zone subject to cyclic injection and implications for injection-induced seismicity. *Geophys. J. Int.,* **232**(3), 1655–1667.

Jiang, Y., Xiao, J., Tanabashi, Y. & Mizokami, T., 2004. Development of an automated servo-controlled direct shear apparatus applying a constant normal stiffness condition. *Int. J. Rock Mech. Min. Sci.,* **41**(2), 275–286.

Keranen, K.M. & Weingarten, M., 2018. Induced Seismicity. *Annu. Rev. Earth planet. Sci.,* **46**(1), 149–174.

Kim, J. & Moridis, G.J., 2015. Numerical analysis of fracture propagation during hydraulic fracturing operations in shale gas systems. *Int. J. Rock Mech. Min. Sci.,* **76,** 127–137.

Kim, K.-H., Ree, J.-H., Kim, Y., Kim, S., Kang, S.Y. & Seo, W., 2018. Assessing whether the 2017 Mw 5.4 Pohang earthquake in South Korea was an induced event. *Science,* **360**(6392), 1007–1009.

Kim, T. & Jeon, S., 2019. Experimental study on shear behavior of a rock discontinuity under various thermal, hydraulic and mechanical conditions. *Rock Mech. Rock Eng.,* **52**(7), 2207–2226.

Kohli, A.H. & Zoback, M.D., 2013. Frictional properties of shale reservoir rocks. *J. geophys. Res.: Solid Earth,* **118**(9), 5109–5125.

Lei, X., Wang, Z. & Su, J., 2019. The December 2018 ML 5.7 and January 2019 ML 5.3 Earthquakes in South Sichuan Basin induced by shale gas hydraulic fracturing. *Seismol. Res. Lett.,* **90**(3), 1099–1110.

Li, Y., Du, X. & Ji, Y., 2022a. Prediction of the transitional normal stress of rock joints under shear. *Int. J. Rock Mech. Min. Sci.,* **159,** 105203, doi:10.1016/j.ijrmms.2022.105203.

Li, Z., *et al.*, 2022b. Induced microearthquakes predict permeability creation in the brittle crust. *Front. Earth Sci.,* **10,** doi:10.3389/feart.2022.1020294.

Logan, J.M., Dengo, C.A., Higgs, N.G. & Wang, Z.Z., 1992. Chapter 2 fabrics of experimental fault zones: their development and relationship to mechanical behavior. In Evans, B. & Wong, T., Eds., *International Geophysics,,* Vol., **51,** pp. 33–67. Academic Press.

Magsipoc, E., Zhao, Q. & Grasselli, G., 2020. 2D and 3D roughness characterization. *Rock Mech. Rock Eng.,* **53**(3), 1495–1519.

Marone, C. & Cox, S.J.D., 1994. Scaling of rock friction constitutive parameters: the effects of surface roughness and cumulative offset on friction of gabbro. *Pure appl. Geophys.,* **143**(1), 359–385.

Marone, C. & Kilgore, B., 1993. Scaling of the critical slip distance for seismic faulting with shear strain in fault zones. *Nature,* **362**(6421), 618–621.

McClure, M. & Horne, R., 2014. Characterizing hydraulic fracturing with a tendency-for-shear-stimulation test. *SPE Reservoir Eval. Eng.,* **17**(02), 233–243.

Melin, H., 2012. Controlling parameters for normal and shear behaviour of rock fractures-a study of direct shear test data from SKB. Retrieved from https://urn.kb.se/resolve?urn=urn:nbn:se:kth:diva-93976. (accessed May 2023).

Morrow, C.A. & Byerlee, J.D., 1989. Experimental studies of compaction and dilatancy during frictional sliding on faults containing gouge. *J. Struct. Geol.,* **11**(7), 815–825.

Murphy, H.D., Grigsby, C.O., Tester, J.W. & Albright, J.N., 1978. *Evaluation of the Fenton Hill Hot Dry Rock Geothermal Reservoir. Part I. Heat Extraction Performance and Modeling. Part II. Flow Characteristics and Geochemistry. Part III. Reservoir Characterization using Acoustic Techniques,* No. LA-UR-78-3143; CONF-781222-1. Los Alamos Scientific Lab., NM, USA. Retrieved from https://www.osti.gov/biblio/6531628. (accessed March 2023).

Niemeijer, A.R. & Spiers, C.J., 2007. A microphysical model for strong velocity weakening in phyllosilicate-bearing fault gouges. *J. geophys. Res.: Solid Earth,* **112**(B10), doi:10.1029/2007JB005008.

Ohnaka, M. & Shen, L., 1999. Scaling of the shear rupture process from nucleation to dynamic propagation: implications of geometric irregularity of the rupturing surfaces. *J. geophys. Res.: Solid Earth,* **104**(B1), 817–844.

Olasolo, P., Juárez, M.C., Morales, M.P., D´Amico, S. & Liarte, I.A., 2016. Enhanced geothermal systems, EGS): a review. *Renew. Sustain. Energy Rev.,* **56,** 133–144. doi: 10.1016/j.rser.2015.11.031.

Orellana, L.F., Giorgetti, C. & Violay, M., 2019. Contrasting mechanical and hydraulic properties of wet and dry fault zones in a proposed shale-hosted nuclear waste repository. *Geophys. Res. Lett.,* **46**(3), 1357–1366.

Rafek, A.G. & Goh, T.L., 2012. Correlation of joint roughness coefficient (JRC) and peak friction angles of discontinuities of Malaysian Schists. *Earth Sci. Res.,* **1**(1), 57, doi:10.5539/esr.v1n1p57.

Rice, J.R., 1975. On the stability of dilatant hardening for saturated rock masses. *J. geophys. Res. (1896-1977),* **80**(11), 1531–1536.

Rice, J.R., 2006. Heating and weakening of faults during earthquake slip. *J. geophys. Res.: Solid Earth,* **111**(B5), doi:10.1029/2005jb004006.

Rudnicki, J.W. & Chen, C.-H., 1988. Stabilization of rapid frictional slip on a weakening fault by dilatant hardening. *J. geophys. Res.: Solid Earth,* **93**(B5), 4745–4757.

Rudnicki, J.W., 2022. Porosity evolution in rate and state friction. *Geophys. Res. Lett.,* **49**(22), e2022GL101056, doi:10.1029/2022GL101056.

Ruina, A., 1983. Slip instability and state variable friction laws. *J. geophys. Res.: Solid Earth,* **88**(B12), 10359–10370.

Rutqvist, J., Freifeld, B., Min, K.-B., Elsworth, D. & Tsang, Y., 2008. Analysis of thermally induced changes in fractured rock permeability during 8 years of heating and cooling at the Yucca Mountain Drift Scale Test. *Int. J. Rock Mech. Min. Sci.,* **45**(8), 1373–1389.

Samuelson, J., Elsworth, D. & Marone, C., 2009. Shear-induced dilatancy of fluid-saturated faults: experiment and theory. *J. geophys. Res.: Solid Earth,* **114**(B12), doi:10.1029/2008JB006273.

Samuelson, J., Elsworth, D. & Marone, C., 2011. Influence of dilatancy on the frictional constitutive behavior of a saturated fault zone under a variety of drainage conditions. *J. geophys. Res.: Solid Earth,* **116**(B10), doi:10.1029/2011JB008556.

Schoenball, M. *et al.*, 2020. Creation of a mixed-mode fracture network at mesoscale through hydraulic fracturing and shear stimulation. *J. geophys. Res.: Solid Earth,* **125**(12), e2020JB019807, doi:10.1029/2020JB019807.

Scholz, C.H., 1988. Mechanisms of seismic quiescences. *Pure appl. Geophys.,* **126**(2), 701–718.

Schultz, R., Skoumal, R.J., Brudzinski, M.R., Eaton, D., Baptie, B. & Ellsworth, W., 2020. Hydraulic fracturing-induced seismicity. *Rev. Geophys.,* **58**(3), e2019RG000695, doi:10.1029/2019RG000695.

Segall, P. & Rice, J.R., 1995. Dilatancy, compaction, and slip instability of a fluid-infiltrated fault. *J. geophys. Res.: Solid Earth,* **100**(B11), 22155–22171.

Segall, P., Rubin, A.M., Bradley, A.M. & Rice, J.R., 2010. Dilatant strengthening as a mechanism for slow slip events. *J. geophys. Res.: Solid Earth,* **115**(B12), doi:10.1029/2010JB007449.

Shapiro, S.A., Huenges, E. & Borm, G., 1997. Estimating the crust permeability from fluid-injection-induced seismic emission at the KTB site. *Geophys. J. Int.,* **131**(2), F15–F18.

Shen, N., Wang, L. & Li, X., 2022. Laboratory simulation of injection-induced shear slip on saw-cut sandstone fractures under different boundary conditions. *Rock Mech. Rock Eng.,* **55**(2), 751–771.

Sibson, R.H., 1985. Stopping of earthquake ruptures at dilational fault jogs. *Nature,* **316**(6025), 248–251.

Sleep, N.H., 1995. Ductile creep, compaction, and rate and state dependent friction within major fault zones. *J. geophys. Res.: Solid Earth,* **100**(B7), 13065–13080.

Sleep, N.H., 2006. Frictional dilatancy. *Geochem. Geophys. Geosyst.,* **7**(10), doi:10.1029/2006GC001374

Snow, D.T., 1969. Anisotropic Permeability of Fractured Media. *Water Resour. Res.,* **5,** 1273–1289. doi: 10.1029/WR005i006p01273.

Tanikawa, W., Sakaguchi, M., Tadai, O. & Hirose, T., 2010. Influence of fault slip rate on shear-induced permeability. *J. geophys. Res.: Solid Earth,* **115**(B7), doi:10.1029/2009JB007013.

Tse, R. & Cruden, D.M., 1979. Estimating joint roughness coefficients. *Int. J. Rock Mech. Min. Sci. Geomech. Abstr.,* **16**(5), 303–307.

Vilarrasa, V. & Carrera, J., 2015. Geologic carbon storage is unlikely to trigger large earthquakes and reactivate faults through which CO2 could leak. *Proc. Natl. Acad. Sci.,* **112**(19), 5938–5943.

Willis-Richards, J., Watanabe, K. & Takahashi, H., 1996. Progress toward a stochastic rock mechanics model of engineered geothermal systems. *J. geophys. Res.: Solid Earth,* **101**(B8), 17481–17496.

Witherspoon, P.A., Wang, J.S.Y., Iwai, K., & Gale,, J.E., 1980. Validity of Cubic Law for fluid flow in a deformable rock fracture. *Water Resour. Res.* **16,** 1016–1024. doi: 10.1029/WR016i006p01016.

Yang, Y. & Dunham, E.M., 2021. Effect of porosity and permeability evolution on injection-induced aseismic slip. *J. geophys. Res.: Solid Earth,* **126**(7), e2020JB021258.

Ye, Z. & Ghassemi, A., 2018. Injection-induced shear slip and permeability enhancement in granite fractures. *J. geophys. Res.: Solid Earth,* **123**(10), 9009–9032.

Yeo, I.W., de Freitas, M.H. & Zimmerman, R.W., 1998. Effect of shear displacement on the aperture and permeability of a rock fracture. *Int. J. Rock Mech. Min. Sci.,* **35**(8), 1051–1070.

Yin, Q., Zhu, C., Wu, J., Pu, H., Wang, Q., Zhang, Y., Jing, H. & Deng, T., 2023. Shear sliding of rough-walled fracture surfaces under unloading normal stress. *J. Rock Mech. Geotech. Eng.,* **15,** 2658–2675. doi: 10.1016/j.jrmge.2023.02.005.

Zang, A., Oye, V., Jousset, P., Deichmann, N., Gritto, R., McGarr, A., Majer, E. & Bruhn, D., 2014. Analysis of induced seismicity in geothermal reservoirs—An overview. *Geothermics,* **52,** 6–21. doi: 10.1016/j.geothermics.2014.06.005.

Zbigniew, M., 1996. Genetic algorithms+ data structures= evolution programs. *Comput. Stat.,* **24,** 372–373. doi: 10.1007/978-3-662-03315-9.

Zhang, S., Ji, Y., Hofmann, H., Yin, Q., Li, S. & Zhang, Y., 2023b. Inversion of mechanical aperture accompanying normal stress unloading caused fracture slip (Version 1). figshare, doi:10.6084/m9.figshare.23995719.v1.

Zhang, S., Ji, Y., Hofmann, H., Zhang, Y., Li, S. & Yin, Q., 2023a. Direct shear tests for natural fractures with different normal stress and surface roughness in sandstone (Version 2). figshare, doi:10.6084/m9.figshare.25408543.v1.

Zhang, X., Jeffrey, R.G. & He, C., 2019a. A numerical model for the effect of permeability change on faulting during fluid injection. *J. geophys. Res.: Solid Earth,* **124**(2), 2080–2101.

Zhao, J., 1997. Joint surface matching and shear strength part A: joint matching coefficient (JMC). *Int. J. Rock Mech. Min. Sci.,* **34**(2), 173–178.

Zhou, C.-B., Chen, Y.-F., Hu, R. & Yang, Z., 2023. Groundwater flow through fractured rocks and seepage control in geotechnical engineering: theories and practices. *J. Rock Mech. Geotech. Eng.,* **15**(1), 1–36.

APPENDIX: TIME HISTORY OF THE NORMAL STRESS UNLOADING TESTS

Fig. A1.

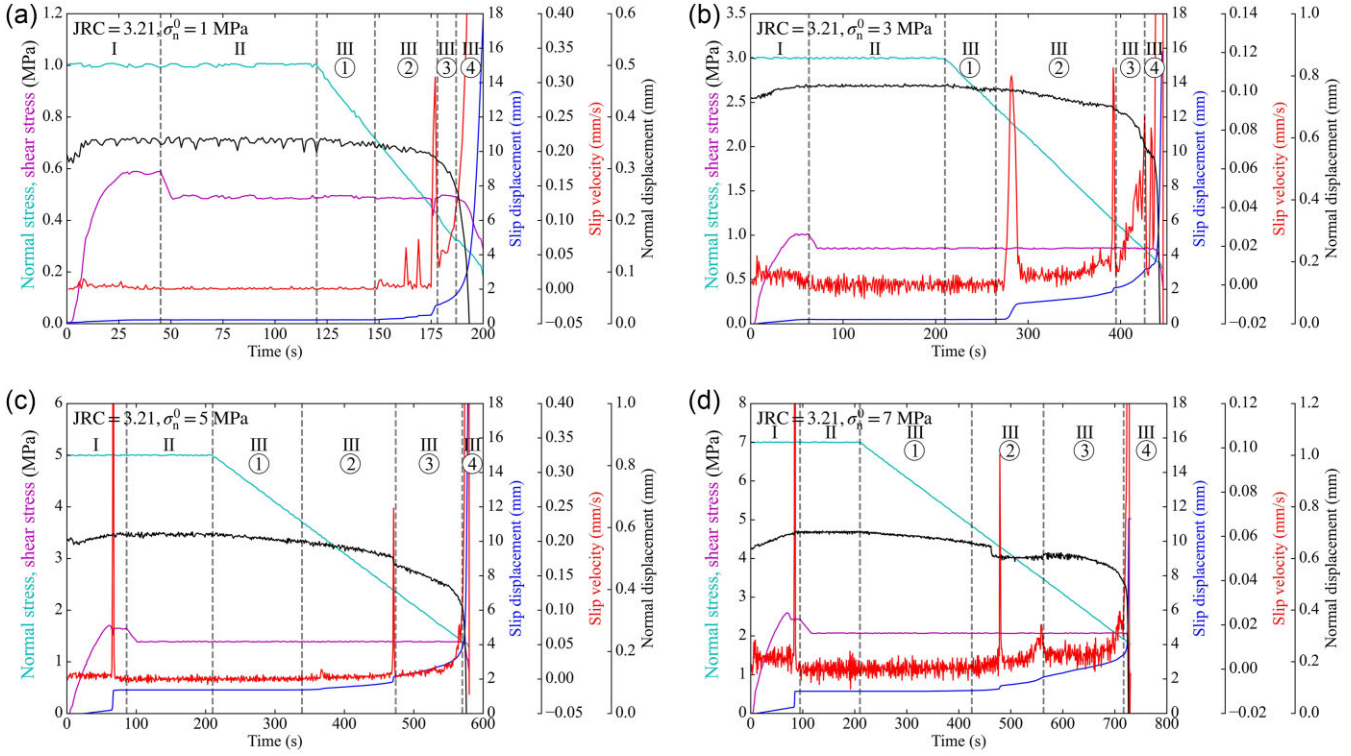

Figure A1. Time histories of the normal stress, shear stress, slip displacement, slip velocity and normal displacement of the 16 normal stress unloading tests. The computations and inversions in this study utilized the data of the first shear cycles of each test (a total of five cycles for each test; Yin *et al.* 2023), except for the three tests under the conditions of (a) JRC = 3.21, σ_n^0 =1 MPa (the second cycle), (i) JRC = 7.36, σ_n^0 =1 MPa (the third cycle), and (j) JRC = 7.36, σ_n^0 =3 MPa (the second cycle). The three exceptions were picked for better data quality and may not impact our analysis and results. The slip velocity is computed as the difference between adjacent slip displacement divided by the time interval. Positive changes in normal displacement indicate normal compaction of the fracture. The grey dashed lines divide the test into three stages, consisting of (I) a displacement-driven shear stage, (II) a shear stress adjustment stage and (III) an unloading-driven shear stage. The unloading-driven shear stage is further divided into four segments, including ① a pre-slip segment, ② a velocity-fluctuation segment, ③ an accelerating slip segment with constant shear stress and ④ an accelerating slip segment with decreasing shear stress. Note that the test (l) with JRC = 7.36 and σ_n^0=7 MPa does not show the velocity-fluctuation segment. The ratio of changes in normal stress and normal displacement in the pre-slip segment was used to estimate the combined normal stiffness of the shear box, rock matrix and fracture in each test. The slip displacement, slip velocity and normal displacement in the accelerating slip segment with constant shear stress in each test were used to constrain the parameters in the displacement- and velocity-dependent aperture models.

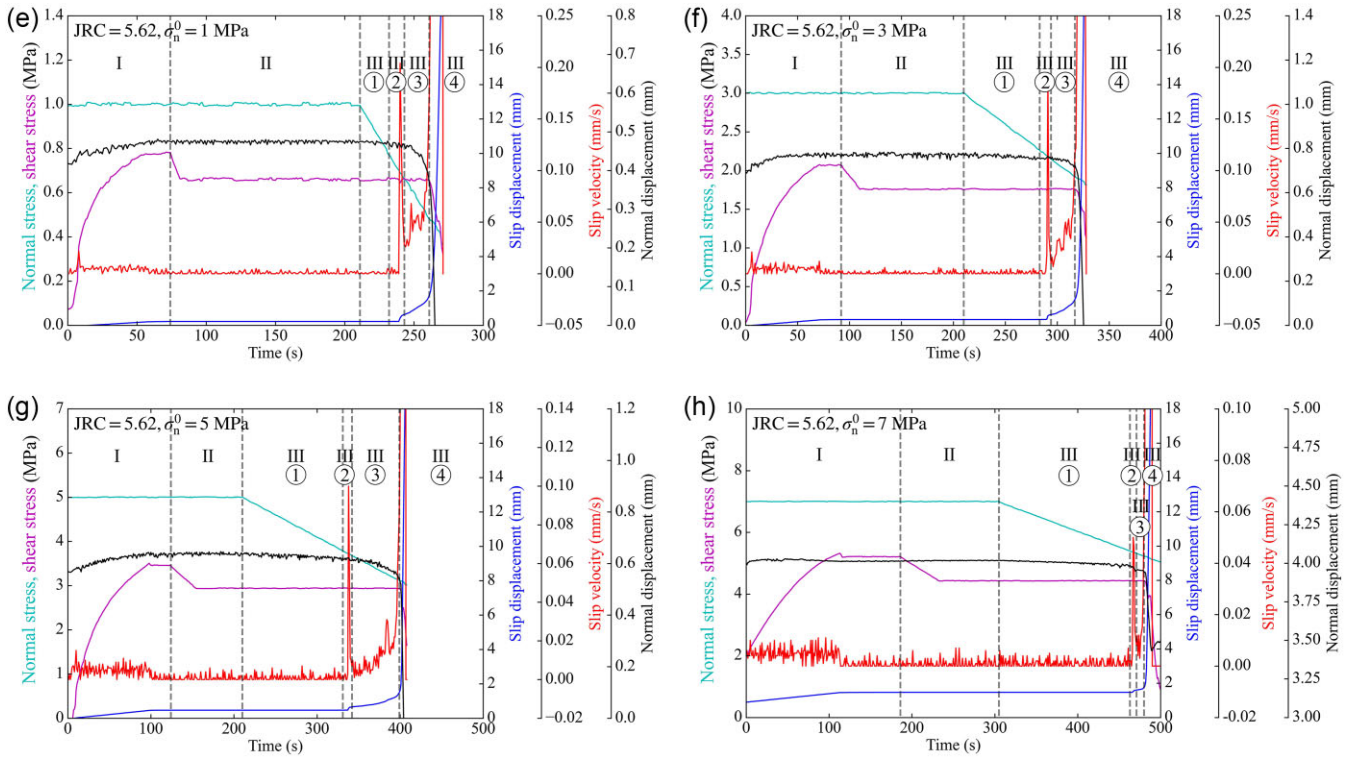

Figure A1. Continued.

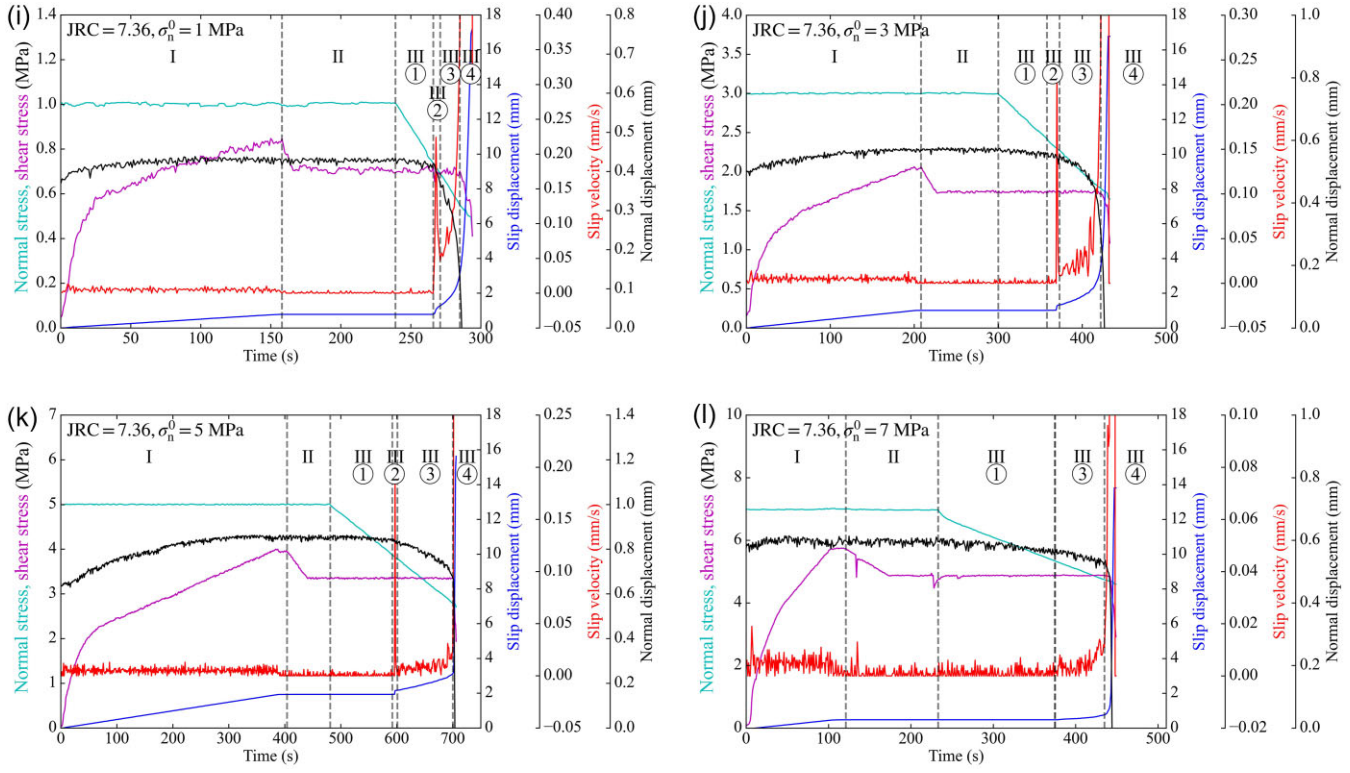

Figure A1. Continued.

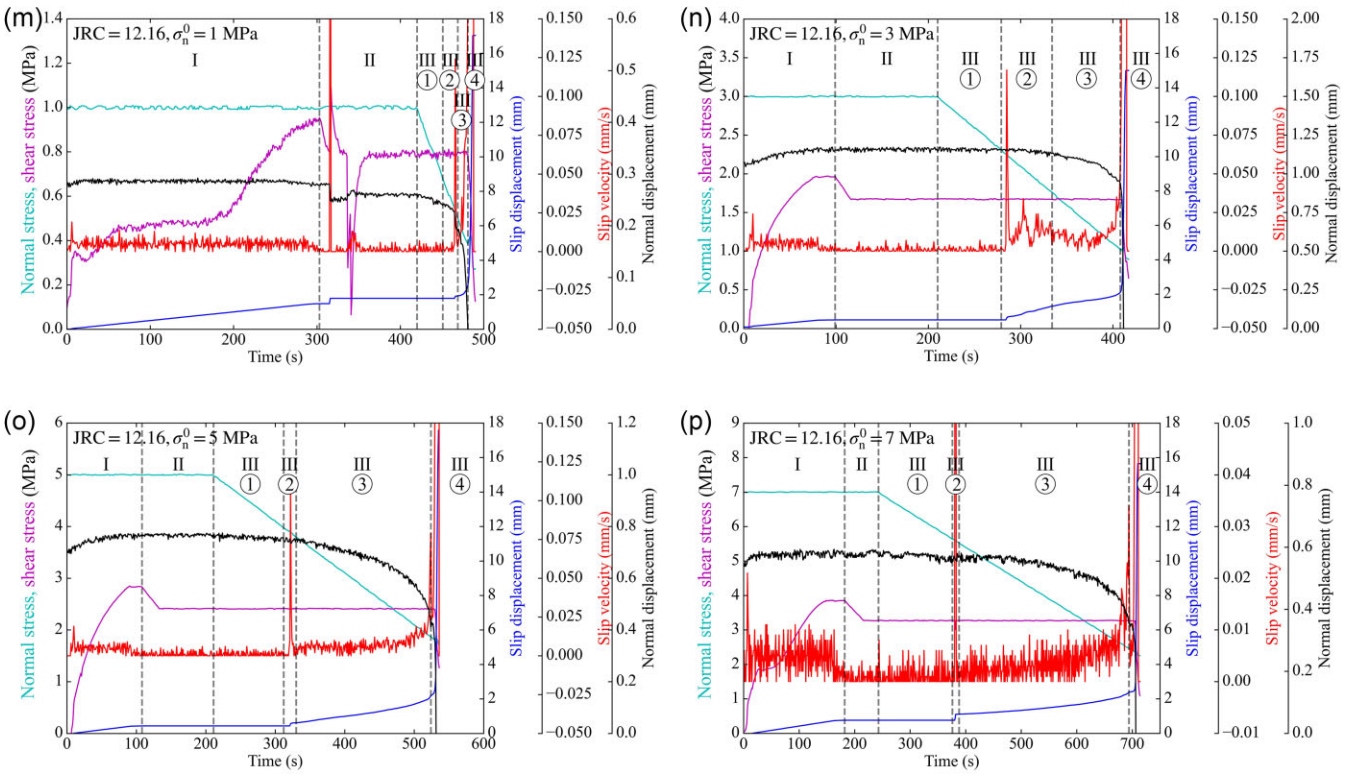

Figure A1. Continued.